

RESEARCH ARTICLE

Probing magneto-ionic microstructure towards the Vela pulsar using a prototype SKA-Low station

C. P. Lee,¹ N. D. R. Bhat,¹ M. Sokolowski,¹ B. W. Meyers,¹ and A. Magro²¹International Centre for Radio Astronomy Research, Curtin University, Bentley, WA 6102, Australia²Institute of Space Sciences and Astronomy, University of Malta, Msida, MSD 2080, Malta

Author for correspondence: C. P. Lee, Email: christopher.lee@icrar.org.

Abstract

The Vela pulsar (J0835–4510) is known to exhibit variations in Faraday rotation and dispersion on multi-decade timescales due to the changing sightline through the surrounding Vela supernova remnant and the Gum Nebula. Until now, variations in Faraday rotation towards Vela have not been studied on timescales less than around a decade. We present the results of a high-cadence observing campaign carried out with the Aperture Array Verification System 2 (AAVS2), a prototype SKA-Low station, which received a significant bandwidth upgrade in 2022. We collected observations of the Vela pulsar and PSR J0630–2834 (a nearby pulsar located outside the Gum Nebula), spanning ~ 1 yr and ~ 0.3 yr respectively, and searched for linear trends in the rotation measure (RM) as a function of time. We do not detect any significant trends on this timescale (\sim months) for either pulsar, but the constraints could be greatly improved with more accurate ionospheric models. For the Vela pulsar, the combination of our data and historical data from the published literature have enabled us to model long-term correlated trends in RM and dispersion measure (DM) over the past two decades. We detect a change in DM of ~ 0.3 cm⁻³ pc which corresponds to a change in electron density of $\sim 10^5$ cm⁻³ on a transverse length scale of ~ 1 –2 AU. The apparent magnetic field strength in the time-varying region changes from 240^{+30}_{-20} μ G to $-6.2^{+0.7}_{-0.9}$ μ G over the time span of the data set. As well as providing an important validation of polarimetry, this work highlights the pulsar monitoring capabilities of SKA-Low stations, and the niche science opportunities they offer for high-precision polarimetry and probing the microstructure of the magneto-ionic interstellar medium.

Keywords: instrumentation: interferometers – techniques: polarimetric – pulsars: individual: PSR J0835–4510, J0630–2834 – ISM: supernova remnants**1. Introduction**

Pulsars are highly-polarised radio sources which have long been used as tools to probe magneto-ionised plasma in the Milky Way and the Local Bubble (e.g., Manchester 1972; Bhat, Gupta, and Rao 1998), the solar wind (e.g., You et al. 2012; Howard et al. 2016), and the terrestrial ionosphere (e.g., Sotomayor-Beltran et al. 2013; Porayko et al. 2019). Propagation through the ionised intervening media imparts frequency-dependent distortions on pulsar signals which can be precisely measured due to the short intrinsic timescales and broadband nature of the signals. Of particular interest are the cold-plasma dispersion and Faraday rotation effects on the received pulsar signal, characterised by the dispersion measure (DM) and rotation measure (RM) respectively. Together, these quantities contain information about the thermal electron density and magnetic field strength along the line of sight. In fact, pulsar observations are exceptionally useful for studying the magneto-ionised interstellar medium (ISM), including the supernova remnants (SNRs) surrounding young pulsars such as the Vela pulsar (e.g., Hamilton, McCulloch, Manchester, et al. 1977; Hamilton, Hall, and Costa 1985) and the Crab pulsar (e.g., Rankin et al. 1988).

There are three standard methods for determining the strength of the magnetic field in the ISM. Zeeman splitting of spectral lines provides both the strength and direction of the magnetic field; however, it is only observable for relatively

strong magnetic fields in H I regions or cold, dense molecular clouds (e.g., Heiles 1976; Heiles 1989). Alternatively, one can determine the magnetic field strength from the intensity of synchrotron emission, which typically requires making an assumption such as equipartition between the energy density of cosmic ray particles and that of the magnetic field (e.g., Beck and Krause 2005; Arbutina et al. 2012; Urošević, Pavlović, and Arbutina 2018). Although the equipartition method is useful when the available data are limited, it is biased towards areas with strong magnetic fields, which leads to estimates which are higher than average (Beck et al. 2003). Lastly, the magnetic field strength can also be inferred from the Faraday rotation of linearly polarised emission, such as from synchrotron sources or pulsars. Using pulsar observations, the mean magnetic field strength parallel to the line of sight is simply

$$\langle B_{\parallel} \rangle \simeq c^{-1} \frac{\text{RM}}{\text{DM}}, \quad (1)$$

where $c^{-1} \approx 1.232$ μ G and the RM and DM are in their conventional units (rad m⁻² and cm⁻³ pc, respectively). A positive $\langle B_{\parallel} \rangle$ indicates that the magnetic field is, on average, pointing towards the observer. This method is biased towards the warm ionised ISM, and can also be biased if small-scale fluctuations in the magnetic field and the electron density are correlated (Beck et al. 2003). However, pulsar observations still provide a relatively accurate way to estimate the line-of-sight magnetic field strength in almost any direction, which makes it possible

to map the large-scale structure of the Galactic magnetic field (e.g., Manchester 1974; Han et al. 2006; Han et al. 2018; Sobey et al. 2019).

Stochastic fluctuations in RM and DM due to turbulence in the ISM are expected to be of the order 10^{-5} – 10^{-4} rad m⁻² for observing campaigns of ~ 1 – 5 yr (Porayko et al. 2019). This is below the sensitivity of current pulsar monitoring campaigns due to the noise floor set by models of the ionospheric RM contribution. However, it is still possible to study long-term deterministic trends in RM and DM, which can arise for a number of reasons. Linear trends are often observed due to the transverse motion of the pulsar, which causes the line of sight to probe different regions of the ISM at different times (e.g., Backer et al. 1993; Hobbs et al. 2004; You et al. 2007; Yan et al. 2011; Jones et al. 2017; Wahl et al. 2022; Keith et al. 2024). Additionally, periodic variations on a ~ 1 yr timescale can arise due to the line of sight probing the solar wind, particularly for pulsars at low solar latitudes (e.g., Jones et al. 2017; Wahl et al. 2022; Tiburzi et al. 2021). Detailed characterisation of these trends is important for reducing red noise in long-term pulsar timing experiments, which is necessary in order to detect the stochastic gravitational wave background (e.g., Reardon et al. 2023; Agazie et al. 2023).

Correlated variations in the measured RM and DM can arise when compact regions of magnetised plasma move through the line of sight. As demonstrated by Hamilton, McCulloch, Manchester, et al. (1977) and Hamilton, Hall, and Costa (1985), the mean magnetic field strength in the time-varying region can be estimated from the gradients of the two measures:

$$\langle B_{\parallel} \rangle_{\text{var}} \simeq \mathcal{C}^{-1} \left(\frac{d\text{RM}}{dt} \right) \left(\frac{d\text{DM}}{dt} \right)^{-1}, \quad (2)$$

where \mathcal{C}^{-1} is as defined in equation (1). Using observations of the Vela pulsar over ~ 15 yr, Hamilton, Hall, and Costa (1985) calculated $\langle B_{\parallel} \rangle_{\text{var}} = 22 \mu\text{G}$, which the authors attribute to a magnetised filament in the Vela SNR moving out of the line of sight. $\langle B_{\parallel} \rangle_{\text{var}}$ has also been estimated for the Crab pulsar ($170 \mu\text{G}$; Rankin et al. 1988) and several other pulsars (see e.g., van Ommen et al. 1997; Yan et al. 2011). More recently, Xue (2019) analysed ~ 50 yr of historical RM and DM measurements towards the Vela pulsar, and identified three separate monotonic trends in the RM: increasing between 1970–1984, decreasing between 1984–2006, then again increasing between 2006–2019. Meanwhile, the DM monotonically decreased over this period, with a flattening in the gradient around 1995 as reported by Petroff et al. (2013). From equation (2), these findings imply that the mean line-of-sight magnetic field through the filament underwent two reversals during this time period. Xue (2019) suggested that this could be explained by an inhomogeneous magnetic field within the filament. Given that the Vela pulsar is embedded in a region of turbulent plasma with an apparently inhomogeneous magnetic field, we expect that there may be measurable structure on shorter timescales than what has already been observed, i.e., months to years.

The SKA-Low will be the most sensitive low-frequency

telescope ever built, enabling studies of nearly the entire Galactic pulsar population (e.g., Keane et al. 2015). In preparation for the construction of the SKA-Low, several prototype ‘stations’ have been deployed at Inyarrimanha Ilgari Bundara, CSIRO’s Murchison Radio-astronomy Observatory (MRO), to assist with engineering development. In this paper, we aim to use one of these stations, the Aperture Array Verification System 2 (AAVS2), to search for temporal changes on timescales of months to years which could arise from magneto-ionic microstructure in the Vela SNR. Additionally, verification of the prototype station polarimetry will be essential for gaining confidence in polarimetric data obtained with the SKA-Low, and analysis of pulsar observations can be an effective way of achieving this (e.g., Xue et al. 2019). The remainder of this paper is organised as follows. In §2, we describe the telescope, source selection, observations, and data reduction. In §3, we describe the methods used to estimate the RM and DM. In §4, we present the results, including polarimetric pulse profiles and the RM and DM measurements. We use these results to validate the station polarimetry and test ionospheric models. In §5, we compare the results with historical data and discuss implications for future low-frequency monitoring science. Finally, in §6, we summarise and present our conclusions.

2. Observations and data reduction

All observations were collected with the AAVS2 (van Es et al. 2020; Macario et al. 2022), a prototype SKA-Low station consisting of 256 dual polarised log-parabolic antennas pseudo-randomly distributed over a circular ground plane with a diameter of ~ 42 m and a maximum baseline of ~ 38 m. The AAVS2 operates in the frequency range 50–350 MHz and records ~ 925.926 kHz wide coarse channels separated by ~ 781.25 kHz in order to avoid the drop in sensitivity towards the edges of the bandpass response. The initial AAVS2 system was only capable of recording data from a single coarse channel at a time, but nevertheless was used to detect 20 pulsars at various frequencies (Lee et al. 2022). In early 2022, the AAVS2 received an upgrade which enabled it to record data from multiple contiguous coarse channels. Although in principle this upgrade enables the simultaneous recording of an arbitrary number of channels, the practical limit is set by the maximum possible data recording rate. In this work, we recorded contiguous frequency bands with 16 and 32 channels, corresponding to instantaneous bandwidths of 12.5 MHz and 25 MHz, respectively. In Table 1, we summarise the frequency setups used and their corresponding effective resolutions in Faraday space as defined in equation (8).

We collected multi-channel observations of PSR J0835–4510 (the Vela pulsar) between 2022-02 and 2022-11 to assist with testing and verification of the upgraded recording system. Using these initial observations, we selected the frequency bands to use for further monitoring. The precision of RM measurements increases at lower frequencies due to the increasing number of rotations of the electric vector over the observing bandwidth. Therefore, we obtain the best precision when observing at the lowest possible frequencies. The Vela pulsar is

Table 1. AAVS2 frequency bands used in this work. The columns (from left to right) are: the centre frequency (ν_{ctr}), the bandwidth ($\Delta\nu$), the span in λ^2 ($\Delta\lambda^2$), the Faraday depth resolution ($\delta\phi$; see equation 8), the number of observations (N_{obs}), and the target pulsar.

ν_{ctr} [MHz]	$\Delta\nu$ [MHz]	$\Delta\lambda^2$ [m ²]	$\delta\phi$ [rad m ²]	N_{obs}	Target
105.859375	12.5	1.91	1.99	30	J0630–2834
205.859375	12.5	0.26	14.73	22	J0835–4510
212.109375	25.0	0.47	8.01	2	J0835–4510
326.171875	12.5	0.06	58.64	27	J0835–4510

heavily scattered at low frequencies, becoming undetectable in beamformed observations below ~ 160 MHz (e.g., Kirsten et al. 2019). Since heavy scattering depolarises and degrades the signal, we selected a frequency range between 199.6 MHz and either 212.1 or 224.6 MHz (for 16 and 32-channel recording bands, respectively). We also selected a higher frequency band between 319.9–332.4 MHz to use for additional validation of the AAVS2 polarimetry, as well as DM measurements. An observing campaign was carried out on the Vela pulsar with a cadence of ~ 1 day–3 weeks (depending on the telescope availability) between 2022–11–21 and 2023–05–23. In this paper, we use the observations from this monitoring campaign, as well as some additional observations in the same frequency ranges which were initially recorded for engineering verification purposes. The observations were typically 15 min in length and collected at transit (~ 18 deg from zenith).

In addition to the Vela pulsar, we collected observations of PSR J0630–2834 in the frequency range 99.6–112.1 MHz. This pulsar has a sky position outside of the Gum Nebula and is strongly polarised with no significant scatter broadening in this frequency band. It also has a high fractional linear polarisation and transits near zenith, making it a good control source for polarimetric verification (e.g., Xue et al. 2019). Five observations were collected at source transit on various dates between 2022–08–14 and 2022–12–09. The remaining observations were collected in sets of nine, where four observations were collected before and after transit in addition to an observation at transit. Three observations were discarded due to problems with the recording system, leaving 24 observations at various angles from zenith.

The beamformed voltages were coherently dedispersed and folded using DSPSR (van Straten and Bailes 2011), and subsequent processing was performed using utilities from PSRCHIVE (Hotan, van Straten, and Manchester 2004; van Straten, Demorest, and Osłowski 2012). The pulsar archives were processed with 256 phase bins (equivalent to a time resolution of 348.93 μs for Vela) and a frequency resolution of 3.617 kHz. The oversampled bandwidth was removed and the coarse channels were combined using psradd. The topocentric folding period and DM were then updated using pdmp and pam, and radio frequency interference (RFI) was excised using paz. The Faraday rotation imparted on each observation was removed using pam.

3. Data analysis

3.1 RM-synthesis

The polarisation state of an electromagnetic wave can be described by the four Stokes parameters (I, Q, U, V), where I is the total intensity, Q and U are the components of linear polarisation, and V is the circular polarisation. The linear polarisation is described by a vector in the complex plane

$$P = Q + iU = pIe^{2i\psi}, \quad (3)$$

where p is the fractional degree of linear polarisation and ψ is the position angle of linear polarisation. Propagation through magnetised plasma rotates the polarisation vector as a function of the observational wavelength (λ) squared. When the polarised signal originates from a single source along the line of sight, the rotation in λ^2 is linearly proportional to the RM, such that

$$\psi = \psi_0 + \text{RM}\lambda^2, \quad (4)$$

where ψ_0 is the intrinsic position angle and

$$\text{RM} = \mathcal{C} \int_{\text{source}}^{\text{observer}} n_e(l) B_{\parallel}(l) dl, \quad (5)$$

where \mathcal{C} is as defined in equation (1), n_e is the electron density (cm^{-3}), B_{\parallel} is the interstellar magnetic field component parallel to the line of sight (μG), and dl is an infinitesimal path length (pc). The traditional approach to finding the RM is to fit a linear model to ψ as a function of λ^2 and measure the gradient. However, in recent years it has become more common to use the method of RM-synthesis (Burn 1966; Brentjens and de Bruyn 2005), which uses a Fourier transform of the polarisation vector to determine the RM. This approach is more reliable for low signal-to-noise observations, and allows for the separation of the astrophysical signal from weakly chromatic instrumental effects (such as leakages between polarisations).

Following Brentjens and de Bruyn (2005), we introduce a weighting function $W(\lambda^2)$ defined as non-zero at every λ^2 where measurements are made and zero elsewhere. We then express the observed complex polarisation vector as $\tilde{P}_i = w_i P(\lambda_i^2)$, where λ_i is the centre wavelength of channel i and $w_i = W(\lambda_i^2)$. The Faraday dispersion function (FDF; also referred to as the Faraday spectrum) is the Fourier transform of the observed complex polarisation vector,

$$\tilde{f}(\phi) \simeq K \sum_{i=1}^N \frac{\tilde{P}_i}{s_i} e^{-2i\phi(\lambda_i^2 - \lambda_0^2)}, \quad (6)$$

where λ_0 is the reference wavelength (as shown by Brentjens and de Bruyn 2005, this is ideally the weighted average of λ_i^2), ϕ is the Faraday depth (a generalisation of RM defined at all points along the line of sight), K is the reciprocal of the sum of all weights, and $s_i = s(\lambda_i^2)$ where $s(\lambda^2) = I(\lambda^2)/I(\lambda_0^2)$ is a function describing the spectral dependence of the total intensity. The FDF represents the polarised flux density at every Faraday depth; it contains a single peak at the RM as long as the polarisation originates from a single source with

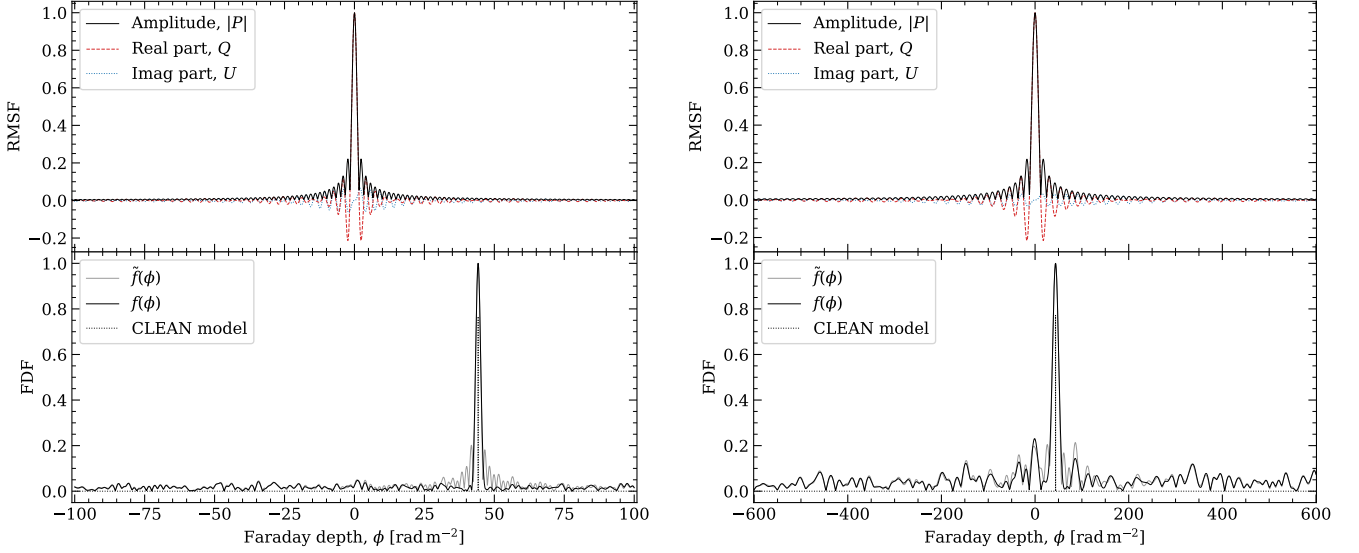


Figure 1. Example RM-synthesis results for observations of J0630–2834 centred at 105.9 MHz (left) and J0835–4510 centred at 205.9 MHz (right). The bandwidth of both observations is 12.5 MHz. Each subfigure shows the following. Top: The RMSF, including the real (Q) and imaginary (U) parts. Bottom: The Faraday spectrum before $[\tilde{f}(\phi)]$ and after $[f(\phi)]$ deconvolution of the RMSF, with the RM-CLEAN model shown. The highest peak in the FDF corresponds to the measured RM, and the smaller peak at $\phi \sim 0 \text{ rad m}^{-2}$ for J0835–4510 is caused by instrumental polarisation.

no internal Faraday rotation (i.e., when the Faraday rotation is proportional to λ^2 as in equation 4). In this paper, we use RM to refer to the measured Faraday depth at the peak of the FDF.

The synthesised FDF in equation (6) is the convolution of the ‘true’ FDF with the RM spread function (RMSF),

$$R(\phi) \simeq K \sum_{i=1}^N w_i e^{-2i\phi(\lambda_i^2 - \lambda_0^2)}. \quad (7)$$

In order to obtain the best signal-to-noise ratio, the RMSF must be deconvolved from the synthesised FDF.

The resolution in Faraday space is determined by the full width at half maximum (FWHM) of the RMSF,

$$\delta\phi \left[\text{rad m}^{-2} \right] = \frac{3.8}{\lambda_{\text{max}}^2 - \lambda_{\text{min}}^2}, \quad (8)$$

where λ_{min} and λ_{max} are the shortest and longest wavelengths in metres, and we use the updated proportionality constant from Schnitzeler, Katgert, and de Bruyn (2009). We then estimate the uncertainty in ϕ as

$$\sigma_\phi = \frac{\delta\phi}{2.355 \times S/N_F}, \quad (9)$$

where S/N_F is the polarised signal-to-noise ratio in the FDF and 2.355 is the conversion between the FWHM and the standard deviation of a Gaussian.

Our analysis was performed using a Python implementation of RM-synthesis and the RM-CLEAN deconvolution algorithm made available as a public repository^a by Heald, Braun, and Edmonds (2009). To measure the RM, the observation

archives were first downsampled to 32 phase bins to increase the signal-to-noise of the Stokes (I , Q , U) spectra per bin. The bin with the highest total intensity was then extracted using `pdv` from `PSRCHIVE`. The Stokes Q and U samples were normalised by the best-fit power-law model to the Stokes I samples as a function of frequency, then combined to form samples of the polarisation vector, $P_i = w_i [Q(\lambda_i) + iU(\lambda_i)]$, using a uniform weighting scheme. For the observations of J0630–2834, the FDF was computed in the Faraday depth range $-100 \leq \phi \leq 100 \text{ rad m}^{-2}$ with a step size of 0.001 rad m^{-2} ; whilst for Vela, we used the range $-600 \leq \phi \leq 600 \text{ rad m}^{-2}$ and a step size of 0.01 rad m^{-2} . These parameter choices ensure that the FDF is oversampled (to precisely locate the peak) and enough off-peak noise is captured for calculating S/N_F . The RMSF was deconvolved from the FDF using an RM-CLEAN component cutoff of $S/N_F = 2$. The RM was then estimated by fitting a parabola to the peak of the FDF and solving for the Faraday depth of the vertex. The S/N_F was calculated as the ratio of the peak in the FDF and the standard deviation of the RM-CLEAN residuals.

Figure 1 shows example FDFs and RMSFs for J0630–2834 and J0835–4510. For both pulsars, the FDF shows a clear peak at the RM of the pulsar. The J0835–4510 FDF shows a small peak at $\phi \sim 0 \text{ rad m}^{-2}$ caused by instrumental polarisation, whilst the J0630–2834 FDF shows no significant instrumental peak. Due to the pristine RFI conditions at the MRO, the observations required very minimal data flagging, particularly in the $\sim 200 \text{ MHz}$ frequency bands. As a result, the theoretical RMSFs are all similar in shape, with a main lobe flanked by increasingly weaker sidelobes. The resolution in Faraday space is significantly smaller for J0630–2834, but in both cases the resolution is high enough to neglect any instrumental polarisation. For the frequency band at 326.17 MHz, the ϕ resolution

a. <https://github.com/gheald/RMtoolkit>

is not sufficient to resolve the RM peak from the instrumental peak, so reliable RM measurements could not be obtained for these observations. Nevertheless, we were able to measure an apparent RM in order to remove the majority of the Faraday rotation from the data.

3.2 Ionospheric RM subtraction

The observed RM (RM_{obs}) can be treated as a sum of the contributions from different Faraday rotating media along the line of sight. The main contributions come from the ionised ISM (RM_{ISM}), the interplanetary medium, and the terrestrial ionosphere (RM_{ion}). In practice, the interplanetary plasma (from solar wind and coronal mass ejections) only needs to be considered for pulsars near the ecliptic (e.g., You et al. 2012), which is not the case for the pulsars studied in this work. We therefore assume the following:

$$RM_{\text{obs}} = RM_{\text{ISM}} + RM_{\text{ion}}. \quad (10)$$

In order to estimate RM_{ISM} , the ionospheric contribution must be modelled and subtracted from RM_{obs} . An ideal ionospheric model must account for variability on a wide range of timescales, including solar flares (on timescales of minutes), diurnal variations (1 day cycle), and the 11 yr solar cycle (e.g., Sotomayor-Beltran et al. 2013; Lam et al. 2016). There are several publicly available software repositories which can be used to estimate RM_{ion} . In this paper, we use the Python package `RMextract`^b (Mevius 2018). We provide a brief summary of the methods implemented in this software below, but further details can be found in Porayko et al. (2023).

For simplicity, it is common practice to approximate the ionosphere as an infinitesimally thin shell of plasma with an effective altitude of between 350–650 km (known as the single layer model or SLM; e.g., Sotomayor-Beltran et al. 2013). The value of RM_{ion} at the intersection of the line of sight and the ionospheric shell, known as the ionospheric pierce point (IPP), is estimated as

$$RM_{\text{ion}} = \eta \text{TEC}_{\text{LOS}} B_{\text{LOS}}, \quad (11)$$

where $\eta = 2.630 \times 10^{-17} \text{ G}^{-1}$, TEC_{LOS} is the slant total electron content at the geographical location of the IPP (m^{-2}) and B_{LOS} is the geomagnetic field strength at the IPP (G). The total electron content (TEC) can be obtained from global ionosphere maps (GIMs) provided by the International GNSS Service (IGS; Hernández-Pajares et al. 2009) via the NASA Archive of Space Geodesy Data^c. There are several GIMs provided by different analysis centres, each sharing data from the same network of IGS ground stations but using different modelling and interpolation methods. Porayko et al. (2019) performed a detailed comparison of several GIMs for the site of the Low-Frequency Array (LOFAR), finding that the best results came from UQRG (from the Technical University of Catalonia; Orús et al. 2005) and JPLG (from the Jet Propulsion Laboratory). Since the accuracy depends on the geographical

coverage of GNSS ground stations, additional verification is required at the MRO. Although a similarly detailed comparison is beyond the scope of this paper, we provide a simple comparison of UQRG and JPLG on SKA-Low station data in §4.2. The geomagnetic field (B_{LOS}) was calculated using the World Magnetic Model (NCEI Geomagnetic Modeling Team and British Geological Survey 2019). Other models are available, however Porayko et al. (2019) found that the difference between models is $\sim 0.1\%$, which is negligible compared to the uncertainties in the ionospheric TEC. `RMextract` spatially interpolates the vertical TEC maps to the IPP using a simple four-point formula (e.g., Schaer 2015). The maps are then computed for the observation epoch using a linear interpolation in time.

As discussed by Porayko et al. (2023), the full electron density profile of the atmosphere includes the plasmasphere, which extends from the top of the ionosphere up to $\sim 20,000$ km in altitude. Since the RM is an integrated quantity, the magnetic field strength gradient over this altitude range can cause an overestimation in the RM determined using the single-layer approximation. To account for this, `RMextract` includes a second method which numerically integrates equation (11) over the electron density and magnetic field strength profiles, then normalises the integral by the vertical TEC values from the GNSS GIMs. The ionospheric density profile is obtained from the International Reference Ionosphere (IRI) model and its extension to plasmaspheric altitudes (IRI-Plas).

Following Sotomayor-Beltran et al. (2013), we used the root-mean-square (RMS) vertical TEC maps to estimate the 1σ uncertainty for each RM_{ion} measurement. Inspection of the estimated uncertainties revealed several outliers ranging from ~ 0.07 – 1.2 rad m^{-2} , whereas the vast majority of points were distributed close to the median value of $\sim 0.2 \text{ rad m}^{-2}$. We therefore opted to use an uncertainty of 0.2 rad m^{-2} for all measurements.

3.3 Determination of DM

To determine the DM, the data was averaged into 8 frequency subbands and a template profile was created by co-adding all of the available observations for the given frequency band. We obtained pulse arrival times for each subband using the Fourier phase gradient algorithm with Markov chain Monte Carlo error estimation, as implemented in the `PSRCHIVE` routine `pat`. We then fit the arrival times to measure the DM using `Tempo2` (Hobbs, Edwards, and Manchester 2006).

4. Results

4.1 Polarimetric pulse profiles

Full-Stokes integrated pulse profiles can provide useful insights into the accuracy and reproducibility of polarimetry. This is particularly important for the AAVS2, a prototype aperture array with novel technologies that are yet to be fully validated. In Figure 2, we present polarimetric pulse profiles for both of the target pulsars. The top row shows the best detections for each frequency band, selected based on the linearly polarised signal-to-noise. The bottom row shows composite

b. <https://github.com/lofar-astron/RMextract>

c. <https://cddis.nasa.gov/archive/gps/products/ionex/>

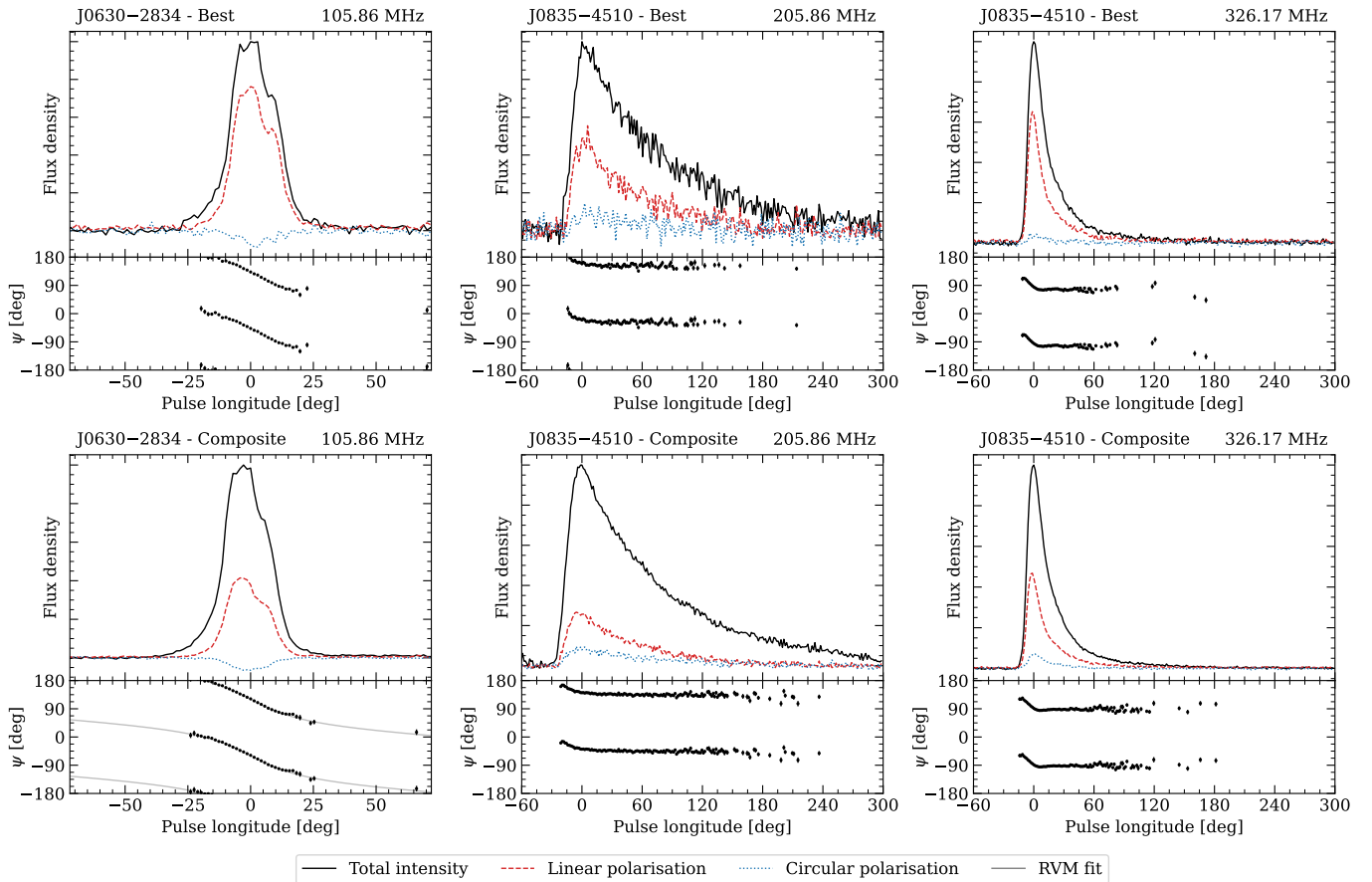


Figure 2. Full-Stokes integrated pulse profiles for J0630–2834 at 105.86 MHz (left); and J0835–4510 at 205.86 MHz (middle) and 326.17 MHz (right). All profiles are processed with 256 phase bins. The top row shows the best single observation based on the linearly polarised signal-to-noise ratio. The bottom row shows composite profiles of all observations in the given frequency band. For each subplot, the top panel shows the pulse profile in total intensity (Stokes I ; black line), linear polarisation (Stokes $\sqrt{Q^2 + U^2}$; red dashed line), and circular polarisation (Stokes V ; blue dotted line). The lower panel shows the position angle for bins with $> 3\sigma$ in linear polarisation. For the composite profile of J0630–2834, the best-fit rotating vector model (RVM) is shown (grey line).

profiles created by phase-aligning and combining all of the integrated pulse profiles with uniform weights using `psradd`. The Faraday rotation was removed for each observation before the profiles were combined. For J0630–2834, the best individual detection is consistent with detections from the Giant Metrewave Radio Telescope (GMRT) at 243 MHz (Johnston *et al.* 2008) and the Murchison Widefield Array (MWA; Tingay *et al.* 2013; Wayth *et al.* 2018) between 140 and 200 MHz (Xue 2019). At 326 MHz, the best individual profile of J0835–4510 is consistent with the detection from Hamilton, McCulloch, Ables, *et al.* (1977) made using Murriyang (CSIRO’s Parkes 64-m radio telescope). At 206 MHz, the best AAVS2 detection is consistent with the full-Stokes profile from the MWA at the same frequency (Xue 2019). The composite profiles display a significantly lower degree of polarisation than the individual observations. This is indicative of some residual error in the polarimetry, which will require further investigation to resolve.

The degree of linear polarisation is expected to be intrinsically stable, which makes it possible to quantify the stability of the polarimetry between observations. For each profile, we measured the fractional degree of linear polarisation (p)

and present the results in Figure 3. For J0630–2834, half of the observations have a fractional polarisation between 0.67 and 0.71, which is similar to what is reported by Johnston *et al.* (2008) and Xue (2019). However, the other half of the observations show a large spread of fractional polarisations, indicating some inconsistency in the quality of the uncalibrated polarimetry. We did not find any significant correlation between the fractional polarisation and the zenith angle, which suggests that the systematic depolarisation is not direction dependent. The fractional polarisations of J0835–4510 are more consistent, with some variance that could be caused by the changing pulse broadening time between observing epochs (e.g., Xue 2019). The range of fractional polarisations are consistent with measurements from Hamilton, McCulloch, Ables, *et al.* (1977) and Xue (2019), with minor discrepancies which could be due to frequency-dependent depolarisation from stochastic fluctuations in the ISM (Burn 1966).

For J0630–2834, we fit the rotating vector model (RVM; Radhakrishnan and Cooke 1969) using `PSRSALSA` (Rooyard, Weltevredde, and Johnston 2015; Weltevredde 2016). We used the routine `ppolFit`, which determines the allowed values of the magnetic inclination angle (α) and the impact parameter

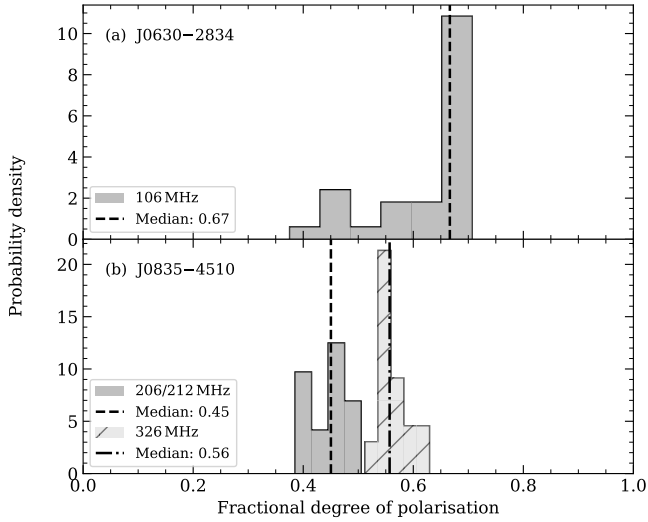


Figure 3. Histograms of the fractional degree of linear polarisation measured from AAVS2 detections. (a) Result for J0630–2834 at 105.86 MHz. (b) Result for J0835–4510 at 205.86/212.11 MHz (dark grey) and 326.17 MHz (light grey, hatched). The median values are indicated by dashed and dot-dashed lines.

(β) by performing a grid search in the α – β parameter space and measuring the reduced χ^2 for each trial. The 68% confidence interval of α and β was determined from the points at which the reduced χ^2 was equal to twice the global minimum. Using the AAVS2 composite profile at 105.86 MHz, we measure $0 \leq \alpha \leq 87.5$ deg and $-13.6 \leq \beta \leq 0$ deg. For comparison, we performed the same analysis on a pulse profile published by Johnston and Kerr (2018) at 1.4 GHz. In this case, we find $0 \leq \alpha \leq 92.8$ deg and $-14.1 \leq \beta \leq 0$ deg. The AAVS2 measurements are therefore consistent with Johnston and Kerr (2018), and place marginally stronger constraints on α and β . In the lower left subplot of Figure 2, we show the RVM fit with the minimum reduced χ^2 ; that is, $\alpha = 0.52$ deg and $\beta = -0.12$ deg.

4.2 Validation of ionospheric models

Due to the large fractional bandwidth, the AAVS2 is capable of determining pulsar RMs with exceptional precision. For our observations of J0630–2834 centred at 106 MHz, 95% of the RM uncertainties are between ~ 0.01 – 0.04 rad m $^{-2}$. For comparison, the 95% confidence lower bound of the distribution of RM uncertainties reported in the ATNF pulsar catalogue (v1.71) is ~ 0.06 rad m $^{-2}$ (Manchester et al. 2005). It is therefore clear that the AAVS2 can determine RM to a precision significantly better than telescopes operating at higher frequencies. This feature makes the AAVS2 well suited for monitoring small variations in ionospheric RM on short timescales (\sim hours), which is useful for testing the accuracy of ionospheric models.

In Figure 4, we present the observed and ionosphere-subtracted RMs for nine observations of J0630–2834 over a ~ 6 h time period on UT+8 2022-10-08. The first four observations were collected before local sunrise, and show small variations of the order ~ 0.01 rad m $^{-2}$ (see the inset in Figure 4). After sunrise, we observe the expected downward trend in

RM_{obs} due to the diurnal photoionisation of the ionosphere. The diurnal trend is the largest source of potential error in the estimated RM of the ISM. Therefore, it is essential that this modulation is properly subtracted. As a simple test, we compare the residual RMs after subtracting the estimated RM_{ion} from two GIMs (JPLG and UQRG) with and without scaling using the IRI-Plas ionospheric density profile (see Figure 4, bottom panel). For reference, we also show the most up to date RM in the ATNF pulsar catalogue (from Johnston et al. 2005).

Since the ISM does not vary appreciably on the timescale of hours, we expect any temporal variations in $RM_{\text{obs}} - RM_{\text{ion}}$ (the ‘residual’ RM) on this timescale to be due to the imperfect subtraction of ionospheric variability. Additionally, because J0630–2834 lies outside of the Gum Nebula, it is not expected show any long-term change in RM. Variations in the residual RM on longer timescales could therefore also be due to the ionospheric model. To quantify these variations, we use the mean absolute deviation^d from the mean of the data. We find that the RM residuals from the single-layer model deviate less than the estimates made using the plasmasphere-extended model (i.e., the single-layer model scaled by the IRI-Plas density profile). Furthermore, we see greater deviations during the daytime hours, especially for the plasmasphere-extended model (see Figure 4). The trend suggests that the plasmasphere-extended model overestimates the ionospheric contribution. Between the two GIMs, we find that JPLG deviates less overall than UQRG, which is due to several significant outliers in the UQRG estimates. The outliers from the UQRG GIM may be a result of the poor GNSS receiver coverage at the MRO, which we discuss further in §5.2. Interestingly, UQRG shows a lower deviation than JPLG when the outliers are excluded. Nevertheless, we use JPLG for all further analysis as it appears to yield more consistent results.

4.3 Temporal RM variations

In Figure 5, we show the complete RM time series for each pulsar before and after subtracting the JPLG/SLM model. To determine the best estimate of RM_{ISM} , we measure the weighted mean of $RM_{\text{obs}} - RM_{\text{ion}}$ by fitting a constant (time-independent) model with a Gaussian likelihood. We set a uniform prior probability and used the Bayesian inference library `Bi1by` to estimate the posterior probability distribution (Ashton et al. 2019). The median and 1, 2, and 3 σ credible intervals of the model fit are shown in Figure 5.

For J0630–2834, we measure a weighted mean of 46.53 ± 0.04 rad m $^{-2}$ (where the uncertainty is the 1 σ credible interval), which is in excellent agreement with the value of 46.53 ± 0.12 rad m $^{-2}$ from Johnston et al. (2005). The RM uncertainties all overlap with the weighted mean of the data, which is indicative that the uncertainties may be overestimated. However, the conservatively large uncertainties account for the lack of knowledge about the accuracy of ionospheric models at the MRO. A linear model fit to the data shows that the gradient is consistent with zero to within 1 σ .

^d. We use the *mean* absolute deviation rather than the *median* absolute deviation so that models with outliers are unfavoured.

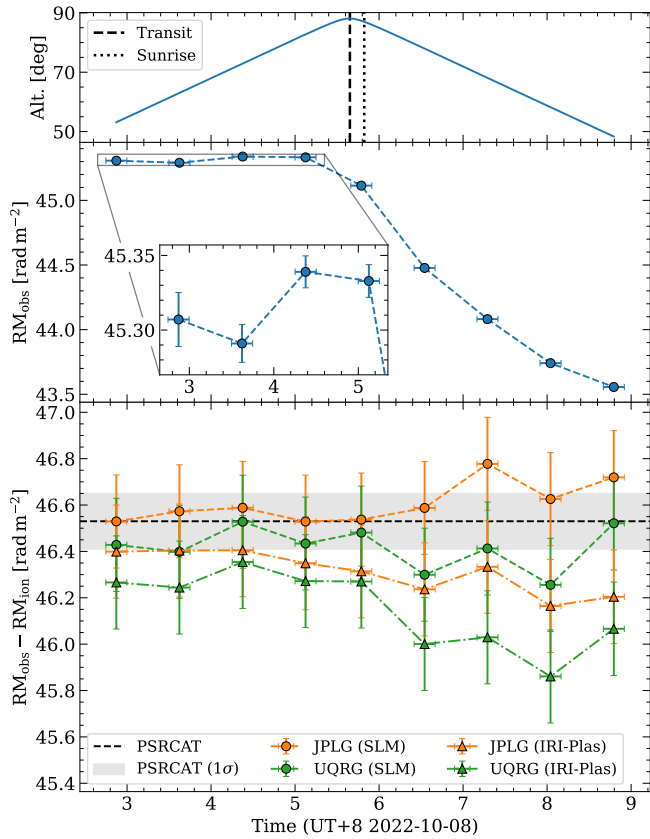


Figure 4. Temporal RM variations towards J0630–2834 over a ~ 6 h period on UT+8 2022-10-08. The top plot shows the source altitude over time, transiting just before sunrise (the time when the Sun reaches an altitude of 0 deg). The middle plot shows the observed RM; the inset shows the small RM variations detected before sunrise. The bottom plot shows the ionosphere-subtracted RMs for JPLG (orange) and UQRG (green) TEC maps with the single-layer model (SLM; circles) and the plasmasphere extended SLM (IRI-Plas; triangles). For reference, we include the RM reported in the ATNF pulsar catalogue from Johnston *et al.* (2005) (black dashed line) and the corresponding uncertainty estimate (grey shaded region).

For J0835–4510, the observed RM decreases over time due to the shift in transit time (and thus the observing time) throughout the year. After subtracting the JPLG/SLM model, we measure a weighted mean RM of 45.57 ± 0.07 rad m^{-2} , which is consistent with the value of 45.3 ± 0.7 rad m^{-2} from Sobey *et al.* (2021). We also observe a residual gradient of -0.8 ± 0.3 $\text{rad m}^{-2} \text{ yr}^{-1}$, which could be the result of a systematic error in the ionospheric model. For example, Porayko *et al.* (2019) observed a systematic error with a period of 1 d in RM residuals after subtracting the JPLG model. This could cause a corresponding error with a period of 1 yr in our data, due to the observations being collected at progressively earlier times of day. An error of this kind would be less significant in the RM series of J0630–2834, which spans only ~ 0.3 yr compared to ~ 1 yr for Vela, and has sparser temporal coverage. If instead we subtract the UQRG/SLM model, we find that the gradient is consistent with zero. The fact that the long-term trend is model dependent is evidence that the trend is systematic in origin, caused by inaccuracies in the JPLG model on an annual timescale. Observations over multiple years will be

required to disentangle model systematics from the underlying astrophysical trend.

4.4 Temporal DM variations

In Figure 6, we show the measured DMs for J0835–4510 from observations at 326.17 MHz. As in §4.3, we fit a constant model with a Gaussian likelihood, and measure a weighted mean value of 67.63 ± 0.01 $\text{cm}^{-3} \text{ pc}$. The time series shows outliers and correlated variability that could be attributed to temporal variations in the pulse broadening time. Such variations can bias the pulse arrival times due to discrepancies between the template profile and the individual observations. A detailed analysis of these variations, including the influence of scattering on the DM measurements, is beyond the scope of this work, and will be deferred to a future publication.

5. Discussion

5.1 Long-term RM and DM variations

The RM and DM of the Vela pulsar have long been observed to change significantly over time, initially showing a correlated linear trend which was attributed to the relative movement of the pulsar and a compact overdensity (filament) of magnetised plasma within the Vela SNR (Hamilton, McCulloch, Manchester, *et al.* 1977). Later analysis of RM measurements published over several decades revealed a more complex deterministic trend; Xue (2019) suggest that the variations in RM could be explained by an inhomogeneous magnetic field within the plasma filament.

In this section, we focus on the most recent two decades of RM and DM variations for the Vela pulsar, which is yet to be analysed in detail in the literature. In Figure 7, we plot all published RM and DM measurements since 2006, including the measurements from this work. From visual inspection of the data, it is immediately apparent that the DM decreased by ~ 0.3 – 0.4 $\text{cm}^{-3} \text{ pc}$ between MJD ~ 56000 (Petroff *et al.* 2013) and MJD ~ 60000 (this work). The sparsity of published data between these dates makes it difficult to disentangle the true change in astrophysical DM with systematic differences due to the profile evolution with frequency and measurement methods. However, the agreement in DM between Murriyang observations at ~ 700 – 4000 MHz (Sobey *et al.* 2021) and MWA observations at ~ 170 – 230 MHz (Xue 2019) collected on similar observing epochs (MJD ~ 58400 – 58900) suggests that the systematic offset arising from the difference in observing frequencies may not be significant to first order. With this in mind, the recent decrease in DM suggests that, contrary to the conclusions of Petroff *et al.* (2013), the filament seen by Hamilton, McCulloch, Manchester, *et al.* (1977) may still be moving out of the line of sight.

Following previous analysis in the literature (e.g. Hamilton, McCulloch, Manchester, *et al.* 1977; Petroff *et al.* 2013; Xue 2019), we fit linear models to measure the gradients in DM and RM over time. Specifically, we consider a simple (one-segment) and a piecewise (two-segment) linear model. Since the RM and DM both depend on the thermal electron density along the line of sight, a significant change in density could

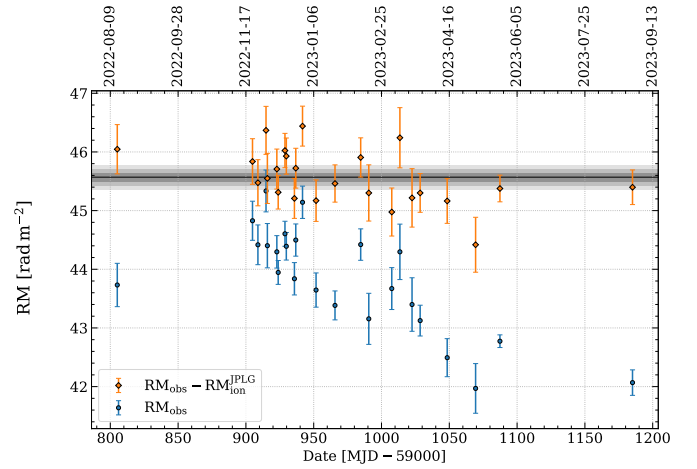
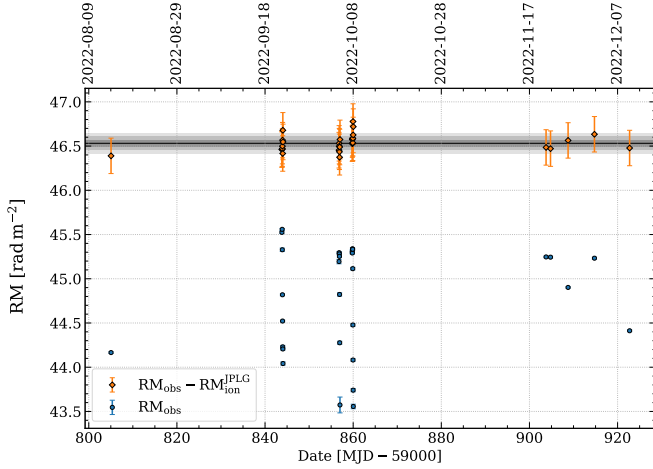


Figure 5. RM time series for J0630–2834 (left) and J0835–4510 (right). Each plot shows the RM before (blue circles) and after (orange diamonds) subtracting the ionospheric RM. We show the weighted mean (black line) of the ionosphere-corrected RM, and the 1, 2, and 3σ credible intervals of the posterior probability distribution (grey shaded bands).

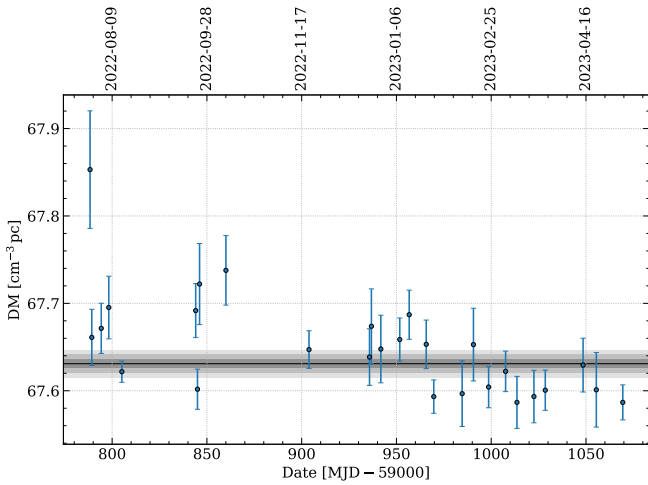


Figure 6. DM time series for J0835–4510. We show the weighted mean (black line) and the 1, 2, and 3σ credible intervals of the posterior probability distribution (grey shaded bands).

result in a correlated change in both quantities. To account for this, we have enforced that the break point in the piecewise model is the same for both the RM and DM. We jointly fit the RM and DM data using a Gaussian likelihood, and make use of the Huber loss function to reduce the weighting of outliers greater than 1.345σ from the model (see Appendix 1 for further details about the model fitting procedure). This approach results in a model fit which is less constrained by measurements with underestimated uncertainties or large systematic offsets from the rest of the data.

In Table 2, we present estimates of the RM and DM gradients and the magnetic field strength computed using equation (2). We estimate each parameter using the median of the posterior distribution, with the uncertainties indicating the 68% credible interval. From the simple linear model fit, we measure $\langle B_{\parallel} \rangle_{\text{var}} = 206^{+23}_{-19} \mu\text{G}$. The piecewise model fit deviates

significantly from the simple model, suggesting that the mean magnetic field in the time-varying region transitions from $240^{+30}_{-20} \mu\text{G}$ to $-6.2^{+0.7}_{-0.9} \mu\text{G}$ at around $\text{MJD } 58050^{+90}_{-100}$. The Bayes factor (i.e. the difference in evidence) between the two model fits is $\log \mathcal{B} = 535.9 \pm 0.2$, which strongly favours the piecewise model. The sign change implies that the mean direction of the magnetic field changes from pointing towards the observer to pointing towards the pulsar. Whilst the estimated magnetic field strengths exceed previous estimates for the Vela pulsar ($\sim 20\text{--}90 \mu\text{G}$; Hamilton, Hall, and Costa 1985; Xue 2019), they are not unreasonable for SNRs. For example, Rankin et al. (1988) measured $\langle B_{\parallel} \rangle_{\text{var}} = 170 \mu\text{G}$ for the Crab pulsar.

Following Hamilton, McCulloch, Manchester, et al. (1977), we can estimate the transverse scale length of the pulsar’s path through the ISM as $\ell = v_{\perp} \Delta t$, where v_{\perp} is the transverse space velocity in pc yr^{-1} and Δt is the time span in years. Assuming a similar scale in the line-of-sight dimension, the excess electron density in the time-varying region (i.e., the change in electron density) is $\Delta n_e = (\text{dDM}/\text{dt})v_{\perp}^{-1}$. The Vela pulsar has a measured transverse velocity of $61 \pm 2 \text{ km s}^{-1}$ (Dodson et al. 2003), or equivalently, $(6.2 \pm 0.2) \times 10^{-7} \text{ pc yr}^{-1}$, placing it at the low end of the velocity distribution for young pulsars (e.g., Lyne and Lorimer 1994). The derived measurements are included in Table 2. We find that the scale lengths of the time-varying regions in the model fits are around $\sim 1\text{--}2 \text{ AU}$. From the simple model fit, we measure an increase in density of $(8.3 \pm 0.8) \times 10^3 \text{ cm}^{-3}$. The piecewise model shows a similar density increase before the break point, followed by a steep decrease of $(1.18 \pm 0.08) \times 10^5 \text{ cm}^{-3}$ after the break point. These density measurements are at least 1–2 orders of magnitude greater than some estimates for bright filaments in the Crab nebula (Osterbrock 1957; Woltjer 1958). Interestingly, the observed structure is comparable in density and length scale with discrete compact structures associated with extreme scattering events in the ISM (e.g., Fiedler et al. 1987; Clegg, Fey, and Lazio 1998; Dong, Petropoulou, and Giannios 2018), which

may reside in old supernova remnants (Romani, Blandford, and Cordes 1987). Of course, another way to reconcile the high implied densities is to consider a structure which is significantly elongated along the line of sight, in which case our measurements would be overestimated. In any case, further observations will be required to better understand the origin of the structure.

One potential cause for a large magnetic field gradient is a compression due to shocks in the ISM. Assuming a simple spherical compression, the magnetic field strength and electron density are positively correlated such that $B \propto n_e^{2/3}$ (e.g., Seta and Federrath 2022). In this case, the decrease in magnetic field strength derived from the piecewise model fit corresponds to a density decrease by a factor of ~ 240 . For a decrease in density of 10^5 cm^{-3} , the final density in the time-varying region is $\sim 420 \text{ cm}^{-3}$. It is important to note that the power-law relation is an idealised model and the true relation is more complex in a turbulent medium (Seta and Federrath 2022).

In the above analysis, we have assumed that the time-varying region is a single compact structure. It is also possible that the observed variations are the result of multiple structures at different locations along the line of sight. In principle, this could be tested by observing interstellar scintillation in Vela pulsar observations at higher frequencies, which can be used to determine the location of one or multiple scattering screens (e.g., Reardon *et al.* 2020). Alternatively, this could be tested via accurate modelling of the pulse shapes at low observing frequencies ($\lesssim 300 \text{ MHz}$), which may necessitate reliably disentangling the profile evolution (in frequency) and frequency-dependent effects of pulse broadening that arise from multipath scattering (e.g., Bhat *et al.* 2004; Geyer *et al.* 2017).

5.2 Implications for future low-frequency pulsar monitoring

The results of this work, and future studies of the magnetionised ISM using the SKA-Low, could be improved with more accurate ionospheric models. Current models are limited by the fact that there is currently only one GNSS ground station at the MRO, with the next nearest stations being 290 and 486 km away. For comparison, the EUREF Permanent GNSS Network^e comprises over 400 GNSS stations distributed throughout Western Europe; ~ 10 of these are within 200 km of the LOFAR core. Having a network of GNSS stations throughout and surrounding the MRO would result in data from more pierce points, which would improve the spacial and temporal resolution of TEC models. In principle, it is also possible to use a widefield interferometer (such as the MWA) to measure refractive shifts in compact radio sources (e.g., Jordan *et al.* 2017), and use these to improve TEC estimates from global models. For monitoring campaigns with multiple target pulsars, calibration observations could be scheduled between pulsar observations to improve the temporal resolution of the TEC estimates. The Phase III capabilities of the MWA may enable this observing strategy. Additionally, the efficiency of pulsar

e. https://epncb.oma.be/_networkdata/stationmaps.php

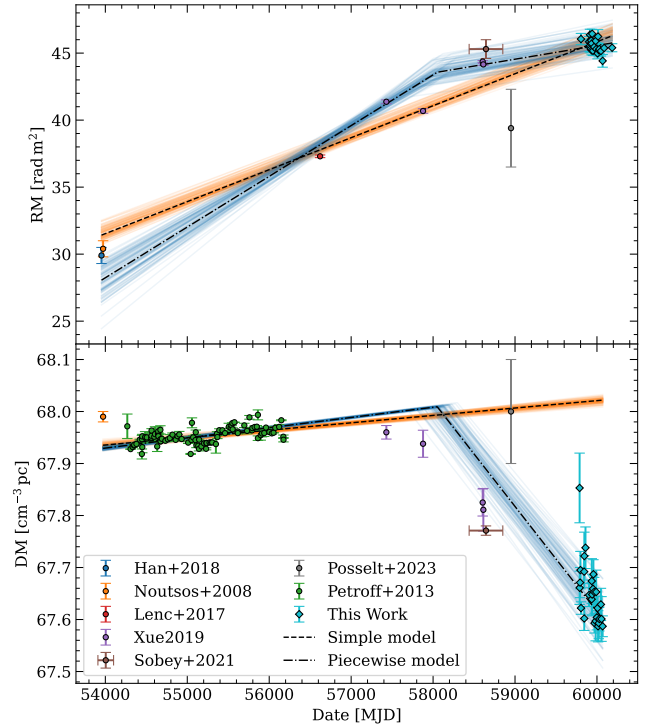


Figure 7. Published measurements of RM (top) and DM (bottom) for J0835–4510 between 2006 and 2023. The black dashed lines show the median simple linear models and the black dot-dashed lines show the median piecewise linear models. The thin orange and blue lines show 100 random samples from the posterior distributions of the simple and piecewise model fits, respectively. The diamond markers show measurements obtained using the AAVS2 in this work; the circle markers show data from Noutsos *et al.* (2008), Petroff *et al.* (2013), Lenc *et al.* (2017), Han *et al.* (2018), Xue (2019), Sobey *et al.* (2021), and Posselt *et al.* (2023). We show horizontal error bars for Sobey *et al.* (2021) as the measurements are averaged over multiple observations (the horizontal uncertainties were not included in the model fits).

monitoring will be significantly improved by the subarray capabilities of the SKA-Low, which could enable simultaneous multi-beamforming and imaging to obtain precise RMs towards a collection of pulsars. The Gum Nebula is a particularly strong science case; as demonstrated by Xue (2019), polarimetric pulsar observations can be used to probe the size and structure of the Nebula.

6. Conclusions

We have analysed low-frequency observations of the Vela pulsar and PSR J0630–2834 collected with the upgraded bandwidth of the AAVS2 prototype station. We find that the polarimetric pulse profiles are consistent with published detections from the MWA, the GMRT, and Murriyang, which is the first validation of pulsar polarimetry from an SKA-Low precursor station. We used the pulsar detections to obtain precise RM estimates for both pulsars, as well as DM estimates for Vela. From a basic comparison of several ionospheric models, we find that the best ionospheric RM estimates come from the JPLG model with a single-layer approximation for the ionospheric shell.

From our observations of Vela, spanning over 1 yr, we ob-

Table 2. Estimated RM and DM gradients and the implied mean magnetic field strength of the magnetised plasma filament. The first row shows the results from a simple linear model; the second and third rows show the results from a piecewise linear model with a variable break point. The columns (from left to right) are: the start and end dates of the linear segment; the transverse scale size probed by the linear model (ℓ); the RM gradient ($d\text{RM}/dt$); the DM gradient ($d\text{DM}/dt$); the mean magnetic field of the time-varying region parallel to the line of sight ($\langle B_{\parallel} \rangle_{\text{var}}$); and the change in electron density (Δn_e). See text for details.

MJD start	MJD end	ℓ	$d\text{RM}/dt$	$d\text{DM}/dt$	$\langle B_{\parallel} \rangle_{\text{var}}$	Δn_e
[day]	[day]	[AU]	[$\text{rad m}^{-2} \text{yr}^{-1}$]	[$10^{-3} \text{cm}^{-3} \text{pc yr}^{-1}$]	[μG]	[10^3cm^{-3}]
53953	60185	2.20 ± 0.07	$0.87^{+0.03}_{-0.04}$	5.2 ± 0.5	206^{+23}_{-19}	8.3 ± 0.8
53953	58050^{+90}_{-100}	1.44 ± 0.06	$1.38^{+0.14}_{-0.11}$	7.2 ± 0.2	240^{+30}_{-20}	11.5 ± 0.5
58050^{+90}_{-100}	60185	$0.75^{+0.05}_{-0.04}$	$0.37^{+0.04}_{-0.03}$	-74 ± 4	$-6.2^{+0.7}_{-0.9}$	-118 ± 8

serve a notable gradient in the RM; however, the temporal sampling is too sparse to confirm an astrophysical origin. More likely, this gradient originates from a systematic error in the ionospheric model. We do not find any significant gradient in RM for PSR J0630–2834, although the shorter time span of the data (~ 0.3 yr) reduces the sensitivity to annual systematics (i.e., those with a period of 1 yr). Further improvements to ionospheric models and a longer-term, higher-cadence observing campaign will be necessary to disentangle systematics from ISM variations on these timescales (\sim months).

By combining our RM and DM data for Vela with published data from 2006 to present, we detect a significant change in DM, and a less significant but correlated change in RM. The temporal variations in this data set probe transverse scale lengths of ~ 1 – 2 AU. We detect a change in the magnetic field strength within the time-varying region from 240^{+30}_{-20} μG to $-6.2^{+0.7}_{-0.9}$ μG , and a corresponding reduction in density by $\sim 10^5 \text{cm}^{-3}$. These measurements suggest the presence of an extremely dense and compact plasma structure, comparable to those associated with extreme scattering events. Further monitoring of RM and DM will provide a useful data set to further investigate microstructure in the ISM towards the Vela pulsar.

Future studies of the ISM using pulsar monitoring could be a niche science opportunity for the MWA and SKA-Low, yielding interesting results from relatively little telescope time. This work highlights the potential for SKA-Low stations to be used for monitoring science, even in the early stages of constructing the SKA-Low. The precision of these studies is currently limited by poorly constrained models of the highly dynamic ionosphere. Further work will be necessary to improve the accuracy of ionospheric RM calibration, either through radio imaging or by expanding the network of GNSS receivers at the MRO.

Acknowledgement

We thank Dejan Urošević for a constructive review which helped to improve this manuscript. We also thank Amit Seta and Poonam Chandra for helpful discussions, Maaijke Mevius for providing ionospheric RM estimates, and Emily Petroff for providing the DM data from Petroff et al. (2013). We acknowledge Riccardo Chiello for his contributions to the TPM firmware. C.P.L. was supported by an Australian Government Research Training Program (RTP) Stipend and RTP Fee-Offset Scholarship. This scientific work makes use of Inyarri-

manha Ilgari Bundara, CSIRO’s Murchison Radio-astronomy Observatory. We acknowledge the Wajarri Yamatji people as the traditional owners of the Observatory site. This work was supported by resources provided by the Pawsey Supercomputing Research Centre with funding from the Australian Government and the Government of Western Australia. The AAVS2 is hosted by the MWA under an agreement via the MWA External Instruments Policy. The acquisition system was designed and purchased by INAF/Oxford University and the RX chain was design by INAF, as part of the SKA design and prototyping program. We acknowledge the support of the Curtin operations team, INAF group, and SKA-Low team in the development and on-going maintenance of the facilities used in this work. This work made use of NASA’s Astrophysics Data System and arXiv.

Software/packages: Astropy (Astropy Collaboration et al. 2018), Bilby (Ashton et al. 2019), corner (Foreman-Mackey 2016), DSPSR (van Straten and Bailes 2011), Dynesty (Speagle 2020), Matplotlib (Hunter 2007), Numpy (Harris et al. 2020), PSRCHIVE (Hotan, van Straten, and Manchester 2004; van Straten, Demorest, and Osłowski 2012), PSRSALSA (Wetvrede 2016), RMextract (Mevius 2018), RMtoolkit (Heald, Braun, and Edmonds 2009), Tempo2 (Hobbs, Edwards, and Manchester 2006).

References

- Agazie, Gabriella, Akash Anumalapludi, Anne M. Archibald, Zaven Arzumian, Paul T. Baker, Bence Bécsy, Laura Blecha, et al. 2023. The NANOGrav 15 yr Data Set: Detector Characterization and Noise Budget. *ApJ* 951, no. 1 (July): L10. <https://doi.org/10.3847/2041-8213/acda88>. arXiv: 2306.16218 [astro-ph.HE].
- Arbutina, B., D. Urošević, M. M. Andjelić, M. Z. Pavlović, and B. Vukotić. 2012. Modified Equipartition Calculation for Supernova Remnants. *ApJ* 746, no. 1 (February): 79. <https://doi.org/10.1088/0004-637X/746/1/79>. arXiv: 1111.5465 [astro-ph.HE].
- Ashton, Gregory, Moritz Hübner, Paul D. Lasky, Colm Talbot, Kendall Ackley, Sylvia Biscoveanu, Qi Chu, et al. 2019. BILBY: A User-friendly Bayesian Inference Library for Gravitational-wave Astronomy. *ApJS* 241, no. 2 (April): 27. <https://doi.org/10.3847/1538-4365/ab06fc>. arXiv: 1811.02042 [astro-ph.IM].
- Astropy Collaboration, A. M. Price-Whelan, B. M. Sipőcz, H. M. Günther, P. L. Lim, S. M. Crawford, S. Conseil, et al. 2018. The Astropy Project: Building an Open-science Project and Status of the v2.0 Core Package. *AJ* 156, no. 3 (September): 123. <https://doi.org/10.3847/1538-3881/aabc4f>. arXiv: 1801.02634 [astro-ph.IM].
- Backer, D. C., S. Hama, S. van Hook, and R. S. Foster. 1993. Temporal Variations of Pulsar Dispersion Measures. *ApJ* 404 (February): 636. <https://doi.org/10.1086/172317>.

- Beck, R., and M. Krause. 2005. Revised equipartition and minimum energy formula for magnetic field strength estimates from radio synchrotron observations. *Astronomische Nachrichten* 326, no. 6 (July): 414–427. <https://doi.org/10.1002/asna.200510366>. arXiv: astro-ph/0507367 [astro-ph].
- Beck, R., A. Shukurov, D. Sokoloff, and R. Wielebinski. 2003. Systematic bias in interstellar magnetic field estimates. *A&A* 411 (November): 99–107. <https://doi.org/10.1051/0004-6361:20031101>. arXiv: astro-ph/0307330 [astro-ph].
- Bhat, N. D. Ramesh, James M. Cordes, Fernando Camilo, David J. Nice, and Duncan R. Lorimer. 2004. Multifrequency Observations of Radio Pulse Broadening and Constraints on Interstellar Electron Density Microstructure. *ApJ* 605, no. 2 (April): 759–783. <https://doi.org/10.1086/382680>. arXiv: astro-ph/0401067 [astro-ph].
- Bhat, N. D. Ramesh, Yashwant Gupta, and A. Pramesh Rao. 1998. Pulsar Scintillation and the Local Bubble. *ApJ* 500, no. 1 (June): 262–279. <https://doi.org/10.1086/305715>. arXiv: astro-ph/9802203 [astro-ph].
- Brentjens, M. A., and A. G. de Bruyn. 2005. Faraday rotation measure synthesis. *A&A* 441, no. 3 (October): 1217–1228. <https://doi.org/10.1051/0004-6361:20052990>. arXiv: astro-ph/0507349 [astro-ph].
- Burn, B. J. 1966. On the depolarization of discrete radio sources by Faraday dispersion. *MNRAS* 133 (January): 67. <https://doi.org/10.1093/mnras/133.1.67>.
- Clegg, Andrew W., Alan L. Fey, and T. Joseph W. Lazio. 1998. The Gaussian Plasma Lens in Astrophysics: Refraction. *ApJ* 496, no. 1 (March): 253–266. <https://doi.org/10.1086/305344>. arXiv: astro-ph/9709249 [astro-ph].
- Dodson, R., D. Legge, J. E. Reynolds, and P. M. McCulloch. 2003. The Vela Pulsar's Proper Motion and Parallax Derived from VLBI Observations. *ApJ* 596, no. 2 (October): 1137–1141. <https://doi.org/10.1086/378089>. arXiv: astro-ph/0302374 [astro-ph].
- Dong, Lingyi, Maria Petropoulou, and Dimitrios Giannios. 2018. Extreme scattering events from axisymmetric plasma lenses. *MNRAS* 481, no. 2 (December): 2685–2693. <https://doi.org/10.1093/mnras/sty2427>. arXiv: 1809.00005 [astro-ph.GA].
- Fiedler, R. L., B. Dennison, K. J. Johnston, and A. Hewish. 1987. Extreme scattering events caused by compact structures in the interstellar medium. *Nature* 326, no. 6114 (April): 675–678. <https://doi.org/10.1038/326675a0>.
- Foreman-Mackey, Daniel. 2016. Corner.py: scatterplot matrices in python. *The Journal of Open Source Software* 1, no. 2 (June): 24. <https://doi.org/10.21105/joss.00024>. <https://doi.org/10.21105/joss.00024>.
- Geyer, M., A. Karastergiou, V. I. Kondratiev, K. Zagkouris, M. Kramer, B. W. Stappers, J. -M. Grießmeier, et al. 2017. Scattering analysis of LOFAR pulsar observations. *MNRAS* 470, no. 3 (September): 2659–2679. <https://doi.org/10.1093/mnras/stx1151>. arXiv: 1706.04205 [astro-ph.HE].
- Hamilton, P. A., P. J. Hall, and M. E. Costa. 1985. Changing parameters along the path to the VELA pulsar. *MNRAS* 214 (May): 5P–8. <https://doi.org/10.1093/mnras/214.1.5P>.
- Hamilton, P. A., P. M. McCulloch, J. G. Ables, and M. M. Komesaroff. 1977. Polarization characteristics of southern pulsars – I. 400–MHz observations. *MNRAS* 180 (July): 1. <https://doi.org/10.1093/mnras/180.1.1>.
- Hamilton, P. A., P. M. McCulloch, R. N. Manchester, J. G. Ables, and M. M. Komesaroff. 1977. Detection of change in rotation measure of the Vela pulsar. *Nature* 265 (January): 224. <https://doi.org/10.1038/265224a0>.
- Han, J. L., R. N. Manchester, A. G. Lyne, G. J. Qiao, and W. van Straten. 2006. Pulsar Rotation Measures and the Large-Scale Structure of the Galactic Magnetic Field. *ApJ* 642, no. 2 (May): 868–881. <https://doi.org/10.1086/501444>. arXiv: astro-ph/0601357 [astro-ph].
- Han, J. L., R. N. Manchester, W. van Straten, and P. Demorest. 2018. Pulsar Rotation Measures and Large-scale Magnetic Field Reversals in the Galactic Disk. *ApJS* 234, no. 1 (January): 11. <https://doi.org/10.3847/1538-4365/aa9c45>. arXiv: 1712.01997 [astro-ph.GA].
- Harris, Charles R., K. Jarrod Millman, Stéfan J. van der Walt, Ralf Gommers, Pauli Virtanen, David Cournapeau, Eric Wieser, et al. 2020. Array programming with NumPy. *Nature* 585, no. 7825 (September): 357–362. <https://doi.org/10.1038/s41586-020-2649-2>. arXiv: 2006.10256 [cs.LG].
- Heald, G., R. Braun, and R. Edmonds. 2009. The Westerbork SINGS survey. II Polarization, Faraday rotation, and magnetic fields. *A&A* 503, no. 2 (August): 409–435. <https://doi.org/10.1051/0004-6361/200912240>. arXiv: 0905.3995 [astro-ph.GA].
- Heiles, C. 1976. The interstellar magnetic field. *ARA&A* 14 (January): 1–22. <https://doi.org/10.1146/annurev.aa.14.090176.000245>.
- Heiles, Carl. 1989. Magnetic Fields, Pressures, and Thermally Unstable Gas in Prominent H I Shells. *ApJ* 336 (January): 808. <https://doi.org/10.1086/167051>.
- Hernández-Pajares, M., J. M. Juan, J. Sanz, R. Orus, A. Garcia-Rigo, J. Feltnes, A. Komjathy, S. C. Schaer, and A. Krankowski. 2009. The IGS VTEC maps: a reliable source of ionospheric information since 1998. *Journal of Geodesy* 83, nos. 3–4 (March): 263–275. <https://doi.org/10.1007/s00190-008-0266-1>.
- Hobbs, G., A. G. Lyne, M. Kramer, C. E. Martin, and C. Jordan. 2004. Long-term timing observations of 374 pulsars. *MNRAS* 353, no. 4 (October): 1311–1344. <https://doi.org/10.1111/j.1365-2966.2004.08157.x>.
- Hobbs, G. B., R. T. Edwards, and R. N. Manchester. 2006. TEMPO2, a new pulsar-timing package – I. An overview. *MNRAS* 369, no. 2 (June): 655–672. <https://doi.org/10.1111/j.1365-2966.2006.10302.x>. arXiv: astro-ph/0603381 [astro-ph].
- Hotan, A. W., W. van Straten, and R. N. Manchester. 2004. PSRCHEIVE and PSRFITS: An Open Approach to Radio Pulsar Data Storage and Analysis. *PASA* 21, no. 3 (January): 302–309. <https://doi.org/10.1071/AS04022>. arXiv: astro-ph/0404549 [astro-ph].
- Howard, T. A., K. Stovall, J. Dowell, G. B. Taylor, and S. M. White. 2016. Measuring the Magnetic Field of Coronal Mass Ejections Near the Sun Using Pulsars. *ApJ* 831, no. 2 (November): 208. <https://doi.org/10.3847/0004-637X/831/2/208>.
- Huber, Peter J. 1964. Robust Estimation of a Location Parameter. *The Annals of Mathematical Statistics* 35, no. 1 (March): 73–101. ISSN: 0003-4851. <https://doi.org/10.1214/aoms/1177703732>. <http://projecteuclid.org/euclid.aoms/1177703732>.
- Hunter, John D. 2007. Matplotlib: a 2d graphics environment. *CSE* 9 (3): 90–95. <https://doi.org/10.1109/MCSE.2007.55>.
- Jankowski, F., W. van Straten, E. F. Keane, M. Bailes, E. D. Barr, S. Johnston, and M. Kerr. 2018. Spectral properties of 441 radio pulsars. *MNRAS* 473, no. 4 (February): 4436–4458. <https://doi.org/10.1093/mnras/stx2476>. arXiv: 1709.08864 [astro-ph.HE].
- Johnston, Simon, G. Hobbs, S. Vigeland, M. Kramer, J. M. Weisberg, and A. G. Lyne. 2005. Evidence for alignment of the rotation and velocity vectors in pulsars. *MNRAS* 364, no. 4 (December): 1397–1412. <https://doi.org/10.1111/j.1365-2966.2005.09669.x>. arXiv: astro-ph/0510260 [astro-ph].
- Johnston, Simon, Aris Karastergiou, Dipanjan Mitra, and Yashwant Gupta. 2008. Multifrequency integrated profiles of pulsars. *MNRAS* 388, no. 1 (July): 261–274. <https://doi.org/10.1111/j.1365-2966.2008.13379.x>. arXiv: 0804.3838 [astro-ph].
- Johnston, Simon, and Matthew Kerr. 2018. Polarimetry of 600 pulsars from observations at 1.4 GHz with the Parkes radio telescope. *MNRAS* 474, no. 4 (March): 4629–4636. <https://doi.org/10.1093/mnras/stx3095>. arXiv: 1711.10092 [astro-ph.HE].

- Jones, M. L., M. A. McLaughlin, M. T. Lam, J. M. Cordes, L. Levin, S. Chatterjee, Z. Arzoumanian, et al. 2017. The NANOGrav Nine-year Data Set: Measurement and Analysis of Variations in Dispersion Measures. *ApJ* 841, no. 2 (June): 125. <https://doi.org/10.3847/1538-4357/aa73df>. arXiv: 1612.03187 [astro-ph.HE].
- Jordan, C. H., S. Murray, C. M. Trott, R. B. Wayth, D. A. Mitchell, M. Rahimi, B. Pindor, P. Procopio, and J. Morgan. 2017. Characterization of the ionosphere above the Murchison Radio Observatory using the Murchison Widefield Array. *MNRAS* 471, no. 4 (November): 3974–3987. <https://doi.org/10.1093/mnras/stx1797>. arXiv: 1707.04978 [astro-ph.IM].
- Keane, E., B. Bhattacharyya, M. Kramer, B. Stappers, E. F. Keane, B. Bhattacharyya, M. Kramer, et al. 2015. A Cosmic Census of Radio Pulsars with the SKA. In *Advancing Astrophysics with the Square Kilometre Array (ASKAP14)*, 40. April. <https://doi.org/10.22323/1.215.0040>. arXiv: 1501.00056 [astro-ph.IM].
- Keith, M. J., S. Johnston, A. Karastergiou, P. Weltevrede, M. E. Lower, A. Basu, B. Posselt, et al. 2024. The Thousand-Pulsar-Array programme on MeerKAT - XIII. Timing, flux density, rotation measure, and dispersion measure time series of 597 pulsars. *MNRAS* 530, no. 2 (May): 1581–1591. <https://doi.org/10.1093/mnras/stae937>. arXiv: 2404.02051 [astro-ph.HE].
- Kirsten, F., N. D. R. Bhat, B. W. Meyers, J. -P. Macquart, S. E. Tremblay, and S. M. Ord. 2019. Probing Pulsar Scattering between 120 and 280 MHz with the MWA. *ApJ* 874, no. 2 (April): 179. <https://doi.org/10.3847/1538-4357/ab0c05>. arXiv: 1903.02087 [astro-ph.HE].
- Lam, M. T., J. M. Cordes, S. Chatterjee, M. L. Jones, M. A. McLaughlin, and J. W. Armstrong. 2016. Systematic and Stochastic Variations in Pulsar Dispersion Measures. *ApJ* 821, no. 1 (April): 66. <https://doi.org/10.3847/0004-637X/821/1/66>. arXiv: 1512.02203 [astro-ph.HE].
- Lee, C. P., N. D. R. Bhat, M. Sokolowski, N. A. Swainston, D. Ung, A. Magro, and R. Chiello. 2022. Spectral analysis of 22 radio pulsars using SKA-Low precursor stations. *PASA* 39 (September): e042. <https://doi.org/10.1017/pasa.2022.40>. arXiv: 2208.07182 [astro-ph.HE].
- Lenc, E., C. S. Anderson, N. Barry, J. D. Bowman, I. H. Cairns, J. S. Farnes, B. M. Gaensler, et al. 2017. The Challenges of Low-Frequency Radio Polarimetry: Lessons from the Murchison Widefield Array. *PASA* 34 (September): e040. <https://doi.org/10.1017/pasa.2017.36>. arXiv: 1708.05799 [astro-ph.IM].
- Lyne, A. G., and D. R. Lorimer. 1994. High birth velocities of radio pulsars. *Nature* 369, no. 6476 (May): 127–129. <https://doi.org/10.1038/369127a0>.
- Macario, Giulia, Giuseppe Pupillo, Gianni Bernardi, Pietro Bolli, Paola Di Ninni, Giovanni Comoretto, Andrea Mattana, et al. 2022. Characterization of the SKA1-Low prototype station Aperture Array Verification System 2. *Journal of Astronomical Telescopes, Instruments, and Systems* 8 (January): 011014. <https://doi.org/10.1117/1.JATIS.8.1.011014>. arXiv: 2109.11983 [astro-ph.IM].
- Manchester, R. N. 1972. Pulsar Rotation and Dispersion Measures and the Galactic Magnetic Field. *ApJ* 172 (February): 43. <https://doi.org/10.1086/151326>.
- . 1974. Structure of the Local Galactic Magnetic Field. *ApJ* 188 (March): 637–644. <https://doi.org/10.1086/152757>.
- Manchester, R. N., G. B. Hobbs, A. Teoh, and M. Hobbs. 2005. The Australia Telescope National Facility Pulsar Catalogue. *AJ* 129, no. 4 (April): 1993–2006. <https://doi.org/10.1086/428488>. arXiv: astro-ph/0412641 [astro-ph].
- Mevius, M. 2018. RMextract. *Astrophysics Source Code Library*, ascl: 1806.024.
- NCEI Geomagnetic Modeling Team and British Geological Survey. 2019. *World Magnetic Model 2020*. NOAA National Centers for Environmental Information. <https://doi.org/10.25921/11v3-da71>.
- Noutsos, A., S. Johnston, M. Kramer, and A. Karastergiou. 2008. New pulsar rotation measures and the Galactic magnetic field. *MNRAS* 386, no. 4 (June): 1881–1896. <https://doi.org/10.1111/j.1365-2966.2008.13188.x>. arXiv: 0803.0677 [astro-ph].
- Orús, R., M. Hernández-Pajares, J. M. Juan, and J. Sanz. 2005. Improvement of global ionospheric VTEC maps by using kriging interpolation technique. *Journal of Atmospheric and Solar-Terrestrial Physics* 67, no. 16 (November): 1598–1609. <https://doi.org/10.1016/j.jastp.2005.07.017>.
- Osterbrock, Donald E. 1957. Electron Densities in the Filaments of the Crab Nebula. *PASP* 69, no. 408 (June): 227. <https://doi.org/10.1086/127053>.
- Petroff, E., M. J. Keith, S. Johnston, W. van Straten, and R. M. Shannon. 2013. Dispersion measure variations in a sample of 168 pulsars. *MNRAS* 435, no. 2 (October): 1610–1617. <https://doi.org/10.1093/mnras/stt1401>. arXiv: 1307.7221 [astro-ph.GA].
- Porayko, N. K., A. Noutsos, C. Tiburzi, J. P. W. Verbiest, A. Horneffer, J. Künsemöller, S. Osłowski, et al. 2019. Testing the accuracy of the ionospheric Faraday rotation corrections through LOFAR observations of bright northern pulsars. *MNRAS* 483, no. 3 (March): 4100–4113. <https://doi.org/10.1093/mnras/sty3324>. arXiv: 1812.01463 [astro-ph.IM].
- Porayko, Nataliya K., Maaijke Mevius, Manuel Hernández-Pajares, Caterina Tiburzi, German Olivares Pulido, Qi Liu, Joris P. W. Verbiest, et al. 2023. Validation of global ionospheric models using long-term observations of pulsar Faraday rotation with the LOFAR radio telescope. *Journal of Geodesy* 97, no. 12 (December): 116. <https://doi.org/10.1007/s00190-023-01806-1>.
- Posselt, B., A. Karastergiou, S. Johnston, A. Parthasarathy, L. S. Oswald, R. A. Main, A. Basu, et al. 2023. The Thousand Pulsar Array program on MeerKAT - IX. The time-averaged properties of the observed pulsar population. *MNRAS* 520, no. 3 (April): 4582–4600. <https://doi.org/10.1093/mnras/stac3383>. arXiv: 2211.11849 [astro-ph.HE].
- Radhakrishnan, V., and D. J. Cooke. 1969. Magnetic Poles and the Polarization Structure of Pulsar Radiation. *Astrophys. Lett.* 3 (January): 225.
- Rankin, Joanna M., Donald B. Campbell, Richard B. Isaacman, and Robert R. Payne. 1988. The Crab nebula : secular variations in the Faraday rotation of the pulsar and the great 1974–1975 scattering event. *A&A* 202 (August): 166–172.
- Reardon, Daniel J., William A. Coles, Matthew Bailes, N. D. Ramesh Bhat, Shi Dai, George B. Hobbs, Matthew Kerr, et al. 2020. Precision Orbital Dynamics from Interstellar Scintillation Arcs for PSR J0437–4715. *ApJ* 904, no. 2 (December): 104. <https://doi.org/10.3847/1538-4357/abbd40>. arXiv: 2009.12757 [astro-ph.HE].
- Reardon, Daniel J., Andrew Zic, Ryan M. Shannon, Valentina Di Marco, George B. Hobbs, Agastya Kapur, Marcus E. Lower, et al. 2023. The Gravitational-wave Background Null Hypothesis: Characterizing Noise in Millisecond Pulsar Arrival Times with the Parkes Pulsar Timing Array. *ApJ* 951, no. 1 (July): L7. <https://doi.org/10.3847/2041-8213/acdd03>. arXiv: 2306.16229 [astro-ph.HE].
- Romani, Roger W., Roger D. Blandford, and James M. Cordes. 1987. Radio caustics from localized interstellar medium plasma structures. *Nature* 328, no. 6128 (July): 324–326. <https://doi.org/10.1038/328324a0>.
- Rookyard, S. C., P. Weltevrede, and S. Johnston. 2015. Constraints on viewing geometries from radio observations of γ -ray-loud pulsars using a novel method. *MNRAS* 446, no. 4 (February): 3367–3388. <https://doi.org/10.1093/mnras/stu2236>. arXiv: 1410.3294 [astro-ph.HE].
- Schaer, Stefan. 2015. *IONEX: The IONosphere Map EXchange Format Version 1.1*. Technical report. Astronomical Institute, University of Berne, Switzerland. <https://gssc.esa.int/wp-content/uploads/2018/07/ionex11.pdf>.

- Schnitzeler, D. H. F. M., P. Katgert, and A. G. de Bruyn. 2009. WSRT Faraday tomography of the Galactic ISM at $\lambda \sim 0.86$ m. I. The GEMINI data set at $(l, b) = (181^\circ, 20^\circ)$. *A&A* 494, no. 2 (February): 611–622. <https://doi.org/10.1051/0004-6361/20078912>. arXiv: 0810.4211 [astro-ph].
- Seta, Amit, and Christoph Federrath. 2022. Turbulent dynamo in the two-phase interstellar medium. *MNRAS* 514, no. 1 (July): 957–976. <https://doi.org/10.1093/mnras/stac1400>. arXiv: 2202.08324 [astro-ph.GA].
- Sobey, C., A. V. Bilous, J. -M. Grießmeier, J. W. T. Hessels, A. Karastergiou, E. F. Keane, V. I. Kondratiev, et al. 2019. Low-frequency Faraday rotation measures towards pulsars using LOFAR: probing the 3D Galactic halo magnetic field. *MNRAS* 484, no. 3 (April): 3646–3664. <https://doi.org/10.1093/mnras/stz214>. arXiv: 1901.07738 [astro-ph.GA].
- Sobey, C., S. Johnston, S. Dai, M. Kerr, R. N. Manchester, L. S. Oswald, A. Parthasarathy, R. M. Shannon, and P. Weltevred. 2021. A polarization census of bright pulsars using the ultrawideband receiver on the Parkes radio telescope. *MNRAS* 504, no. 1 (June): 228–247. <https://doi.org/10.1093/mnras/stab861>. arXiv: 2103.13838 [astro-ph.HE].
- Sotomayor-Beltran, C., C. Sobey, J. W. T. Hessels, G. de Bruyn, A. Noutsos, A. Alexov, J. Anderson, et al. 2013. Calibrating high-precision Faraday rotation measurements for LOFAR and the next generation of low-frequency radio telescopes. *A&A* 552 (April): A58. <https://doi.org/10.1051/0004-6361/201220728>. arXiv: 1303.6230 [astro-ph.IM].
- Speagle, Joshua S. 2020. DYNESTY: a dynamic nested sampling package for estimating Bayesian posteriors and evidences. *MNRAS* 493, no. 3 (April): 3132–3158. <https://doi.org/10.1093/mnras/staa278>. arXiv: 1904.02180 [astro-ph.IM].
- Tiburzi, C., G. M. Shaifullah, C. G. Bassa, P. Zucca, J. P. W. Verbiest, N. K. Porayko, E. van der Wateren, et al. 2021. The impact of solar wind variability on pulsar timing. *A&A* 647 (March): A84. <https://doi.org/10.1051/0004-6361/202039846>. arXiv: 2012.11726 [astro-ph.HE].
- Tingay, S. J., R. Goeke, J. D. Bowman, D. Emrich, S. M. Ord, D. A. Mitchell, M. F. Morales, et al. 2013. The Murchison Widefield Array: The Square Kilometre Array Precursor at Low Radio Frequencies. *PASA* 30 (January): e007. <https://doi.org/10.1017/pasa.2012.007>. arXiv: 1206.6945 [astro-ph.IM].
- Urošević, Dejan, Marko Z. Pavlović, and Bojan Arbutina. 2018. On the Foundation of Equipartition in Supernova Remnants. *ApJ* 855, no. 1 (March): 59. <https://doi.org/10.3847/1538-4357/aaac2d>. arXiv: 1801.10422 [astro-ph.HE].
- van Es, A. J. J., M. G. Labate, M. F. Waterson, J. Monari, P. Bolli, D. Davidson, R. Wayth, et al. 2020. A prototype model for evaluating SKA-LOW station calibration. In *Ground-based and Airborne Telescopes VIII*, edited by Heather K. Marshall, Jason Spyromilio, and Tomonori Usuda, 11445:1144589. Society of Photo-Optical Instrumentation Engineers (SPIE) Conference Series. December. <https://doi.org/10.1117/12.2562391>.
- van Ommen, T. D., F. D'Alessandro, P. A. Hamilton, and P. M. McCulloch. 1997. Polarimetric observations of southern pulsars at 800 and 950 MHz. *MNRAS* 287, no. 2 (May): 307–327. <https://doi.org/10.1093/mnras/287.2.307>.
- van Straten, W., and M. Bailes. 2011. DSPSR: Digital Signal Processing Software for Pulsar Astronomy. *PASA* 28, no. 1 (January): 1–14. <https://doi.org/10.1071/AS10021>. arXiv: 1008.3973 [astro-ph.IM].
- van Straten, Willem, Paul Demorest, and Stefan Osłowski. 2012. Pulsar Data Analysis with PSRCHIVE. *Astronomical Research and Technology* 9, no. 3 (July): 237–256. <https://doi.org/10.48550/arXiv.1205.6276>. arXiv: 1205.6276 [astro-ph.IM].
- Wahl, H. M., M. A. McLaughlin, P. A. Gentile, M. L. Jones, R. Spiewak, Z. Arzoumanian, K. Crowter, et al. 2022. The NANOGrav 12.5 yr Data Set: Polarimetry and Faraday Rotation Measures from Observations of Millisecond Pulsars with the Green Bank Telescope. *ApJ* 926, no. 2 (February): 168. <https://doi.org/10.3847/1538-4357/ac4045>. arXiv: 2104.05723 [astro-ph.SR].
- Wayth, Randall B., Steven J. Tingay, Cathryn M. Trott, David Emrich, Melanie Johnston-Hollitt, Ben McKinley, B. M. Gaensler, et al. 2018. The Phase II Murchison Widefield Array: Design overview. *PASA* 35 (November): e033. <https://doi.org/10.1017/pasa.2018.37>. arXiv: 1809.06466 [astro-ph.IM].
- Weltevred, P. 2016. Investigation of the bi-drifting subpulses of radio pulsar B1839-04 utilising the open-source data-analysis project PSRSALSA. *A&A* 590 (May): A109. <https://doi.org/10.1051/0004-6361/201527950>. arXiv: 1605.06413 [astro-ph.HE].
- Woltjer, L. 1958. The Crab nebula. *Bull. Astron. Inst. Netherlands* 14 (January): 39.
- Xue, Mengyao. 2019. Characterising the Local Interstellar Medium using Low-Frequency Pulsar Polarimetry. PhD diss., Curtin Institute of Radio Astronomy, November. <http://hdl.handle.net/20.500.11937/80645>.
- Xue, Mengyao, S. M. Ord, S. E. Tremblay, N. D. R. Bhat, C. Sobey, B. W. Meyers, S. J. McSweeney, and N. A. Swainston. 2019. MWA tied-array processing II: Polarimetric verification and analysis of two bright southern pulsars. *PASA* 36 (July): e025. <https://doi.org/10.1017/pasa.2019.19>. arXiv: 1905.00598 [astro-ph.HE].
- Yan, W. M., R. N. Manchester, G. Hobbs, W. van Straten, J. E. Reynolds, N. Wang, M. Bailes, et al. 2011. Rotation measure variations for 20 millisecond pulsars. *Ap&SS* 335, no. 2 (October): 485–498. <https://doi.org/10.1007/s10509-011-0756-0>. arXiv: 1105.4213 [astro-ph.SR].
- You, X. P., W. A. Coles, G. B. Hobbs, and R. N. Manchester. 2012. Measurement of the electron density and magnetic field of the solar wind using millisecond pulsars. *MNRAS* 422, no. 2 (May): 1160–1165. <https://doi.org/10.1111/j.1365-2966.2012.20688.x>. arXiv: 1202.2263 [astro-ph.SR].
- You, X. P., G. Hobbs, W. A. Coles, R. N. Manchester, R. Edwards, M. Bailes, J. Sarkissian, et al. 2007. Dispersion measure variations and their effect on precision pulsar timing. *MNRAS* 378, no. 2 (June): 493–506. <https://doi.org/10.1111/j.1365-2966.2007.11617.x>. arXiv: astro-ph/0702366 [astro-ph].

Appendix 1. Model fitting methodology

We consider two models for the RM and DM as a function of time. The first is a simple (single-segment) linear model,

$$f_1(t; m, c) = mt + c, \quad (12)$$

where t is the time, m is the gradient, and c is the vertical intercept. The second is a piecewise (two-segment) linear model,

$$f_2(t; m_1, m_2, t_b, c) = m_2t + (m_1 - m_2)t_b + c, \quad (13)$$

where m_1 and m_2 are the gradients of the first and second segment, and t_b is the break point between the segments.

Since the data set contains measurements from different telescopes at different observing frequencies, systematic errors will be inconsistent between publications. To address an analogous issue for pulsar flux density spectra, Jankowski et al. (2018) defined a robust log-likelihood which uses the

Huber loss function to reduce the sensitivity to outlier data points (Huber 1964). The robust log-likelihood is defined as

$$\log \mathcal{L}(y_i; t_i, \Theta) = - \sum_{i=1}^N \begin{cases} \frac{1}{2} \left(\frac{y_i - f(t_i; \Theta)}{\sigma_{y,i}} \right)^2 & \text{if } \left| \frac{y_i - f(t_i; \Theta)}{\sigma_{y,i}} \right| < k \\ k \left| \frac{y_i - f(t_i; \Theta)}{\sigma_{y,i}} \right| - \frac{1}{2} k^2 & \text{otherwise} \end{cases}, \quad (14)$$

where $f(t_i; \Theta)$ is the model, Θ are the model parameters, (t_i, y_i) are the data, $\sigma_{y,i}$ are the uncertainties on y_i , and k is a parameter defining the point at which outlier data points are penalised. Following Huber (1964), we used $k = 1.345$.

We jointly fit the RM and DM datasets by combining the likelihoods, forming a total likelihood

$$\log \mathcal{L} = \log \mathcal{L}_{\text{RM}} + \log \mathcal{L}_{\text{DM}}. \quad (15)$$

For the piecewise linear model, \mathcal{L}_{RM} and \mathcal{L}_{DM} both depend on the break-point parameter t_b , so the RM and DM models are covariant.

We used Bayesian inference to estimate the model parameters and their uncertainties. For the vertical intercepts and the break point, the priors were set to be uniform within the span of the dataset, and zero elsewhere. For the gradients $d\text{RM}/dt$ and $d\text{DM}/dt$, the priors were chosen to be uniform in the ranges $[-5, 5] \text{ rad m}^{-2} \text{ yr}^{-1}$ and $[-0.5, 0.5] \text{ cm}^{-3} \text{ pc yr}^{-1}$, respectively. We used the Dynesty dynamic nested sampler (Speagle 2020) integrated within Bilby (Ashton et al. 2019) to simultaneously estimate the Bayesian evidence and the posterior probability distribution. We then tested the sensitivity of the calculated evidence to the chosen priors by varying the size of the prior space.

The posterior distributions of the fit parameters and $\langle B_{\parallel} \rangle_{\text{var}}$ are shown in Figures 8 and 9.

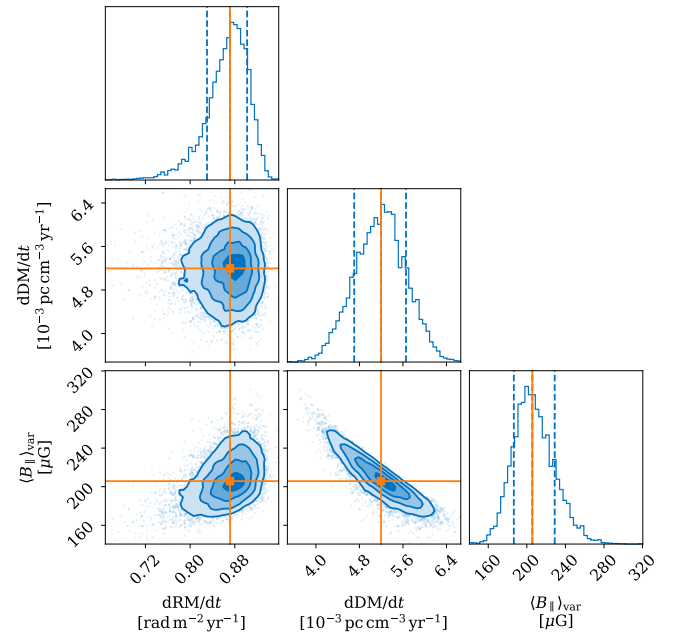


Figure 8. Posterior distributions for the simple linear model fit. The orange lines indicate the median and the blue dashed lines indicate the 16% and 84% percentiles of 1D posterior distributions. The contours indicate the 11.8%, 39.3%, 67.5%, and 86.4% percentiles of the 2D posterior distributions.

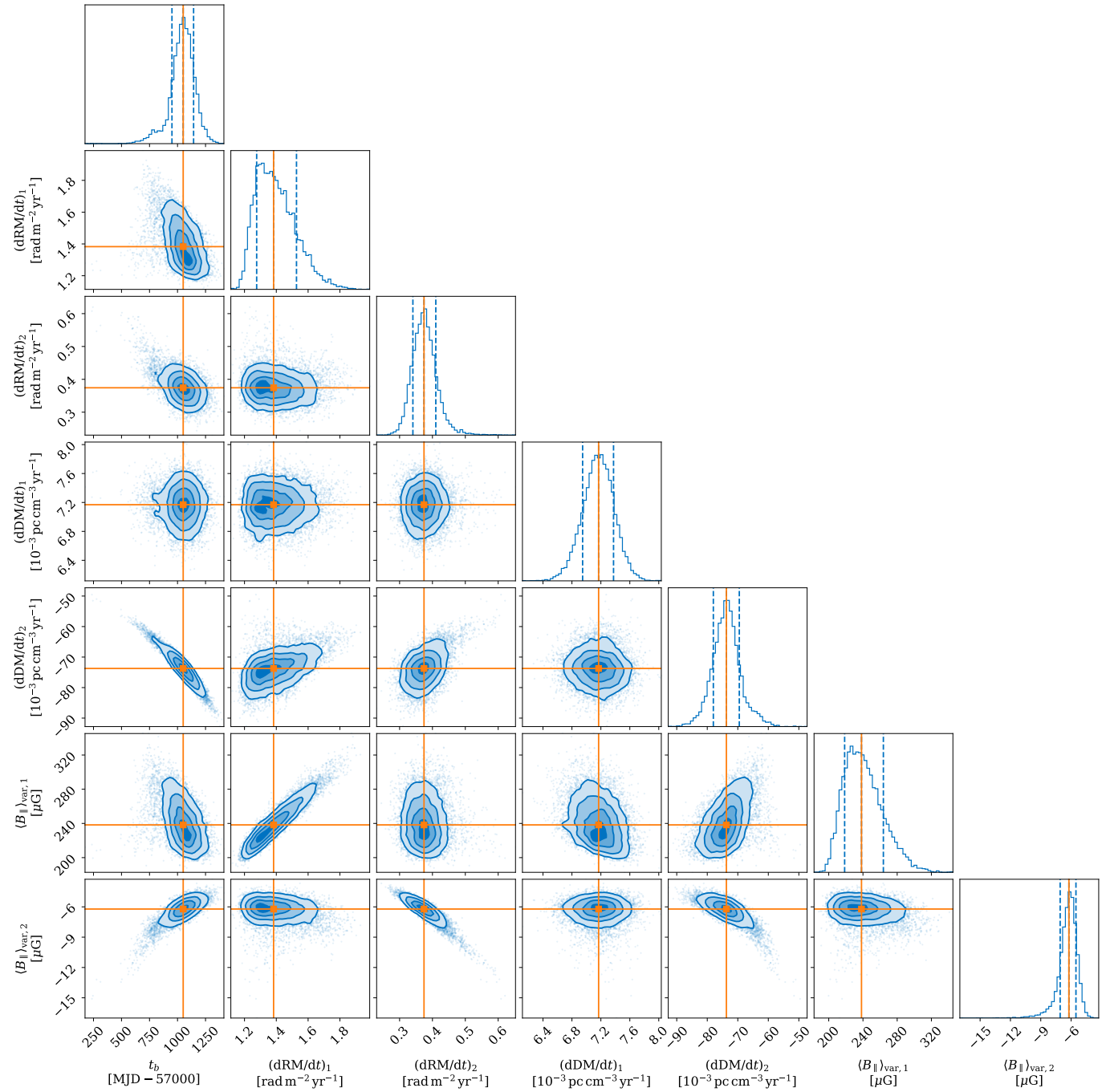


Figure 9. Posterior distributions for the piecewise linear model fit. The orange lines indicate the median and the blue dashed lines indicate the 16% and 84% percentiles of 1D posterior distributions. The contours indicate the 11.8%, 39.3%, 67.5%, and 86.4% percentiles of the 2D posterior distributions.